Nucleosynthesis in thermonuclear supernovae with tracers: convergence and variable mass particles

I. R. Seitenzahl[1], F. K. Röpke[1], M. Fink[1], R. Pakmor[1]

[1] *Max-Planck-Institut für Astrophysik, 85741 Garching, Germany*

28 May 2010

ABSTRACT

Nucleosynthetic yield predictions for multi-dimensional simulations of thermonuclear supernovae generally rely on the tracer particle method to obtain isotopic information of the ejected material for a given supernova simulation. We investigate how many tracer particles are required to determine converged integrated total nucleosynthetic yields. For this purpose, we conduct a resolution study in the number of tracer particles for different hydrodynamical explosion models at fixed spatial resolution. We perform hydrodynamic simulations on a co-expanding Eulerian grid in two dimensions assuming rotational symmetry for both pure deflagration and delayed detonation Type Ia supernova explosions. Within a given explosion model, we vary the number of tracer particles to determine the minimum needed for the method to give a robust prediction of the integrated yields of the most abundant nuclides. For the first time, we relax the usual assumption of constant tracer particle mass and introduce a radially varying distribution of tracer particle masses. We find that the nucleosynthetic yields of the most abundant species (mass fraction $> 10^{-5}$) are reasonably well predicted for a tracer number as small as 32 per axis and direction – more or less independent of the explosion model. We conclude that the number of tracer particles that were used in extant published works appear to have been sufficient as far as integrated yields are concerned for the most copiously produced nuclides. Additionally we find that a suitably chosen tracer mass distribution can improve convergence for nuclei produced in the outer layer of the supernova where the constant tracer mass prescription suffers from poor spatial resolution.

Key words: nuclear reactions, nucleosynthesis, abundances – supernovae: general

1 INTRODUCTION

The basic processes of Type Ia supernovae (SNe Ia) have been proposed almost 50 years ago (see e.g. Hillebrandt & Niemeyer 2000, for a review): A thermonuclear explosion in electron-degenerate matter (Hoyle & Fowler 1960) produces radioactive ^{56}Ni that by its decay delivers energy at exactly the rate observed in SN Ia light curves (Pankey 1962; Truran et al. 1967; Colgate & McKee 1969; Kuchner et al. 1994). Despite this long history, the questions of the progenitor system and the explosion scenario are not completely answered. Pure deflagrations in Chandrasekhar-mass white dwarfs, currently somewhat disfavoured for their apparent inability to produce bright explosions, have been one of the contending explosion scenarios for a long time (e.g. Nomoto et al. 1984; Gamezo et al. 2003; Röpke et al. 2007). If the initial deflagration can transition into a detonation (e.g. Khokhlov et al. 1997; Röpke 2007; Woosley 2007;

Woosley et al. 2009), then better agreement of the models with observations can be obtained (e.g. Röpke & Niemeyer 2007; Bravo & García-Senz 2008; Kasen et al. 2009). If such a deflagration to detonation transition does not occur (cf. e.g. Niemeyer 1999), the possibility that off-center ignition in a single spot leads to a detonation of a white dwarf out of hydrostatic equilibrium in the so-called GCD model is yet another proposed mechanism (Plewa et al. 2004; Jordan et al. 2008; Meakin et al. 2009), although the robustness of the initiation of the detonation in this model is also far from certain (cf. Röpke et al. 2007; Seitenzahl et al. 2009a,b). However, there are indications from recent stellar population synthesis studies (e.g. Ruiter et al. 2009; Mennekens et al. 2010) and X-ray observations of elliptical galaxies and galaxy bulges (Gilfanov & Bogdán 2010), that the long favoured single degenerate Chandrasekhar-mass progenitor channel is unable to account for observational rates of SNe Ia (Cappellaro et al. 1999). Supernovae resulting from the merger of two white dwarfs (e.g. Pakmor et al.

2010) have more favourable statistics and remain a possible explosion channel. Last but not least, the double detonation sub-Chandrasekhar mass model, which has received renewed interest of late (Fink et al. 2007, 2010; Sim et al. 2010), is currently again considered a serious alternative.

The different nucleosynthesis occurring in all these explosion scenarios is an important test for the validity of the respective models. For one-dimensional simulations, the nucleosynthesis can be calculated during the simulation via the coupling of a nuclear reaction network to the hydrodynamics. Since today's most promising explosion models either explicitly break spherical symmetry (e.g. mergers, double detonations, off-center ignitions) or, in the case of centrally ignited spherically symmetric explosions include buoyancy driven turbulent combustion, at least two-dimensional simulations are required to simulate the essential physics of the explosion. Unfortunately, in highly resolved two-dimensional simulations and especially in three-dimensional simulations use of an extended, full nuclear reaction network during the hydrodynamic evolution is computationally not feasible. Consequently, the nuclear energy release for multi-dimensional simulations is modeled with simplified and approximate schemes (e.g. Khokhlov 1995; Reinecke et al. 2002a; Vladimirova et al. 2006; Calder et al. 2007; Townsley et al. 2007; Seitenzahl et al. 2009c). Although some works on multi-dimensional explosion simulations of SN Ia do not calculate any detailed nucleosynthesis at all (e.g. Reinecke et al. 2002b; Plewa et al. 2004; Gamezo et al. 2005; Plewa 2007; Jordan et al. 2008; Bravo & García-Senz 2008), a detailed isotopic composition of the ejecta is often determined in a post-processing step (Travaglio et al. 2004, 2005; Brown et al. 2005; Röpke et al. 2006; Fink et al. 2010; Maeda et al. 2010). While alternative methods for obtaining isotopic nucleosynthetic yields for SNe Ia are currently under investigation (Seitenzahl et al. 2008; Meakin et al. 2009), the tracer particle method still remains currently the only viable choice for the task. In Section 2 we briefly review the tracer particle method and introduce how we distribute tracer particles of variable mass in our initial models. In Section 3 we give details about our hydrodynamic simulations. Section 4 presents the results of a convergence study in the number of tracer particles and highlights the advantages of using a radially varying distribution of tracer masses. We conclude the paper with a summary and discussion in Section 5.

2   TRACER PARTICLE METHOD

Tracer particles are a Lagrangian component in an Eulerian grid code. The particles are assigned masses and positioned in such a way that a density profile reconstructed from their distribution resembles that of the underlying star. During the hydrodynamical simulation, they are advected by the flow, recording the history of thermodynamic conditions along their path. The tracers are nevertheless considered *massless* in the sense that the mass they represent does not couple to the hydrodynamic flow via gravity or inertia – they are simply passively advected by the flow along streamlines.

The tracer particle method in multiple dimensions was employed first by Nagataki et al. (1997) in the context of core collapse supernovae (note that Thielemann et al. (1986)

already post-processed Lagrangian mass zones of 1D hydrodynamical calculations of SNe Ia).

2.1   Tracer particle masses and placement

Historically, N tracer particles are placed in a star of radius R and mass M, such that each tracer particle represents the same amount of mass $m = M/N$. However, other choices for the distribution of tracer masses are possible and may be sometimes preferable. In this paper we consider a tracer mass distribution that varies *smoothly* with radius and additionally fulfills the following criteria:

$$
\begin{aligned}
\text{for} \quad & 0 < \; r \; < R_1 \; : \quad \text{const. mass per particle} \\
\text{for} \quad & R_1 < \; r \; < R_2 \; : \quad \text{const. volume per particle} \quad (1) \\
\text{for} \quad & R_2 < \; r \; < R \; : \quad \text{const. mass per particle,}
\end{aligned}
$$

where $0 < R_1 < R_2 < R$.

This choice of the functional form of the radial distribution of the tracer particles is motivated by the following considerations: in the inner part of the star ($0 < r < R_1$) the burning occurs at high density and tracer particles of constant mass are sufficiently spatially dense to resolve the abundance gradients. In a transition zone ($R_1 < r < R_2$), where the density is lower and nuclear burning is incomplete, intermediate mass elements are synthesized. Due to the relatively low density, a constant tracer mass approach results in a small spatial density of particles there. The constant volume requirement effectively moves tracers from the well sampled inner regions to regions of lower initial density where interesting nucleosynthesis occurs. Finally, a constant volume approach all the way out to the surface of the star would result in a wastefully large amount of tracer particles placed into the very outer layers at very low density where usually no nucleosynthesis occurs. The transition back to constant tracer masses in the very outer layers where hardly any nucleosynthesis occurs ($R_2 < r < R$) alleviates this problem.

In the case of equally massive tracer particles, the white dwarf is divided into N_r shells of equal mass. Then the same number of tracers, N_θ, is distributed uniformly in mass into each of these shells. If the tracers should represent the same volume, the shells are chosen to have the same volume instead. The distribution of the tracers in these shells is done uniformly in mass as before. If both approaches are mixed as described above, we require in addition that the tracers on either side of the interface between the areas of equal-mass and equal-volume all have the same mass. Together with the constraints (1), this leads to the following linear equations constraining the particle numbers N_1, N_2, N_3 in each of the three regions:

$$
\begin{aligned}
\frac{M_1}{N_1} &= \frac{V \rho_1}{N_2} \\
\frac{M - M_2}{N_3} &= \frac{V \rho_2}{N_2} \quad (2) \\
N_1 + N_2 + N_3 &= N_r \,,
\end{aligned}
$$

where $M_i = M(R_i)$ is the enclosed mass as a function of radius, $\rho_i = \rho(R_i)$ is the mass density at position R_i and $V = [4\pi(R_2^3 - R_1^3)]/3$.
Note that for a cold WD in hydrostatic equilibrium of known
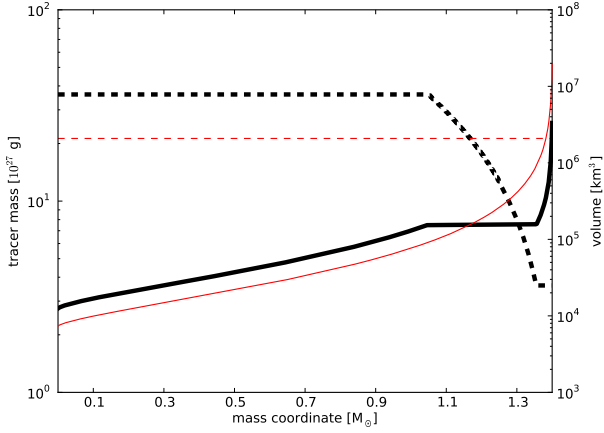
Figure 1. Shown are the mass (dashed lines) and volume (solid lines) represented by a tracer particle as a function of its initial position in the mass coordinate for $N = 256 \times 512$ tracers. Thin (red) lines are for constant tracer particle mass. Thick (black) lines are for variable tracer particle mass for $M_1 = 1.05 \, M_\odot$ and $M_2 = 1.355 \, M_\odot$.

composition and total mass M, given any one of the quantities $\{R_i, M_i, \rho_i\}$ the other two are uniquely determined by the equation of state.

The solution to the set of linear equations (2) is given by:

$$
\begin{aligned}
N_1 &= \frac{A}{A + B + 1} N_r \\
N_2 &= \frac{B}{A + B + 1} N_r \\
N_3 &= \frac{1}{A + B + 1} N_r ,
\end{aligned}
\qquad (3)
$$

where $A = M_1/(V\rho_1)$ and $B = (M - M_2)/(V\rho_2)$.

The tracers are placed into the star according to the rules outlined above. An additional small offset is added to the coordinates such that each particle has a random initial position within its corresponding fluid element. A comparison of the constant and variable tracer mass distributions (for the same number of total tracer particles) is shown in Fig. 1. It is evident from the figure that, for this particular choice of $M_1 = 1.05 \, M_\odot$ and $M_2 = 1.355 \, M_\odot$, in the outer regions of the star $(M(r)/M_\odot \gtrsim 1.15)$ the variable tracer mass approach results in a smaller volume represented by each particle. This increased spatial resolution at low density comes at the expense of slightly larger particle masses in the inner regions of the star.

3 SIMULATIONS

The code used to simulate the supernova explosions is the MPA SN Ia code (see, e.g., Reinecke et al. 1999, 2002a). In this Eulerian hydrodynamics code the reactive Euler equations are solved using a finite volume scheme based on the PROMETHEUS code by Fryxell et al. (1989) which is an implementation of the "piecewise parabolic method" (PPM) of Colella & Woodward (1984). In order to track the expanding WD during explosion, a co-expanding uniform grid as in Röpke & Hillebrandt (2005), and Röpke (2005) is used.

Nuclear burning is included applying a simplified scheme (Reinecke et al. 2002a; Fink et al. 2010): level sets are used to propagate the nuclear burning flames at the correct speed. In this thin flame approximation, an immediate energy release is performed behind the level set representing the flame surface using the new tables from Fink et al. (2010) for detonations. A table for deflagrations was calculated similar to that work.

All simulations presented here were performed assuming 2D rotational symmetry on a grid with cylindrical coordinates. The initial stellar model was a cold, isothermal ($T = 5 \times 10^5 \, \mathrm{K}$) white dwarf in hydrostatic equilibrium of mass $M_{WD} = 1.401 \, M_\odot$ and electron fraction $Y_e = 0.49886$, which corresponds to a central density of $\rho_c = 2.9 \times 10^9 \, \mathrm{g \, cm^{-3}}$. For nuclear energy generation purposes, the composition was assumed to be 50% ^{16}O and 50% ^{12}C by mass homogeneously throughout the star. The grid resolution was 512×512 cells for simulations that were restricted to one hemisphere (assuming mirror symmetry across the equator), and 512×1024 cells for simulations that included both hemispheres respectively. Three different sets of explosion models were investigated. They are discussed briefly in turn below.

3.1 Centrally ignited pure deflagration

In the pure turbulent deflagration model, the burning was ignited centrally in a simple spherical shape of radius 150 km with a superposed two-period cosine-wave perturbation of amplitude 30 km (the C3 ignition configuration as described by Reinecke et al. 1999). This setup assumed mirror symmetry across the equator. This explosion produced $\sim 0.45 \, M_\odot$ of iron group elements (IGE).

3.2 Centrally ignited delayed detonation

In the second model, an initial deflagration was ignited centrally in exactly the same C3 configuration as in the pure deflagration runs (see above). This time, the deflagration transitioned to a detonation after the flame had entered the distributed burning regime and the Karlovitz number[1] exceeded 250 (see Kasen et al. 2009). This setup also assumed mirror symmetry across the equator. This explosion produced $\sim 0.57 \, M_\odot$ of IGE.

3.3 Multi point ignition delayed detonation

For the third set of explosion simulations, the deflagration was ignited in 100 ignition kernels of radius 6 km randomly drawn from a Gaussian radial distribution with a standard deviation of 150 km and from a uniform distribution in angle, resulting in ignition kernels distributed within the inner 306 km of the WD core (corresponding to the ignition model DD2D_iso_06 of Kasen et al. 2009). The detonation was triggered in the same way as the centrally ignited delayed detonation described above. This setup simulated both

---

[1] The use of the Karlovitz number is not rigorous here as it depends on the concept of a laminar flame speed which does not exist in the distributed burning regime. Nonetheless, it is formally used in order to characterize the strength of turbulence.

hemispheres independently and represented a full star in axisymmetry. This explosion produced $\sim 1.03\, M_\odot$ of IGE.

3.4 Post-processing

In the post-processing step, isotopic nucleosynthetic yields for 384 nuclides are calculated by integration of a nuclear reaction network over the recorded temperature and density time histories along the paths the tracer particles took in the hydrodynamic simulation. Apart from the added feature to allow for variable tracer particle masses (see section 2.1), the post-processing scheme is identical to the one used in Fink et al. (2010), which in turn is based on Travaglio et al. (2004). Further detailed description of how the code solves the nuclear network can be found in Thielemann et al. (1990), Thielemann et al. (1996), and Iwamoto et al. (1999). For the reaction rate libraries we use the 2009 release of REACLIB (Rauscher & Thielemann 2000), and for the weak reaction rates we use (Langanke & Martinez-Pinedo 2000). For post-processing purposes, it was assumed that the initial composition of the unburned material was a homogeneous mix consisting of 50% ^{16}O, 47.5% ^{12}C, and 2.5% ^{22}Ne by mass (to account for solar metalicity of the ZAMS progenitor).

4 CONVERGENCE STUDY

An important question to ask is how many tracer particles are needed to converge on the final integrated mass fractions after freeze-out. Only a limited amount of work has been done so far in this direction. Travaglio et al. (2004) performed in the context of core collapse supernova models a 1D resolution study on the number of tracer particles and conclude that for 2000 zones convergence is reached at 1000 particles. They stated that the results may not be applicable in the multi-dimensional case and that a resolution study for 2D is in preparation, which, however, apparently was not published. Brown et al. (2005) post-processed a 2D pure deflagration explosion with 10000 (constant mass) tracer particles. They found, that when choosing a random subset of 5000 tracer particles, the ^{56}Ni mass changed by 8% (they didn't state whether it increased or decreased). Most recently Röpke et al. (2006), post-processed 3D pure deflagration models with 27^3 tracer particles in the productions runs. They looked into variations of the ^{56}Ni mass by increasing the number of tracers to 35^3 and concluded that differences were on the percent level. To date, a more detailed study spanning a larger range of tracer particle number and including isotopes different from ^{56}Ni has not been done.

Here we present a more thorough resolution study in the number of tracer particles for the three different explosion models outlined in Section 3. For the pure deflagration (see Section 3.1) and the centrally ignited delayed detonation simulations (see Section 3.2) we have calculated nucleosynthetic yields based on 64, 256, 1024, 4096, 16384 and 65536 constant mass tracer particles. For the multi-point ignition delayed detonation (see Section 3.3), which did not assume mirror symmetry across the equator, we have calculated nucleosynthetic yields based on 128, 512,

2048, 8192, 32768 and 131072 constant mass tracer particles. This corresponds in all cases to 8, 16, 32, 64, 128, and 256 tracer particles per axis and direction. In addition, we have calculated yields for the same multi-point ignition delayed detonation model with variable tracer masses using $M_1 = 1.05\, M_\odot$ and $M_2 = 1.355\, M_\odot$ as introduced in Section 2.1. For the variable tracer mass case the total numbers of tracers were slightly different[2], i.e. 122, 499, 2024, 8140, 32664, and 130865. For practical purposes these numbers can be considered to be the same resolution.

In this paper we are less concerned with the exact magnitude of the mass fraction of a given nuclide, but rather with how well the yields of the run that included the most tracer particles are reproduced by a run with fewer tracer particles and how quickly the various mass fractions converge with total tracer particle number.

In Figs. 2 and 3 we show, for sequences of runs with increasing tracer particle numbers, percent differences of nuclide mass fractions compared to the mass fractions obtained in the run that included the highest number of tracer particles, which serve as "reference values". To visually emphasize nuclides with larger mass fractions, the symbol radius, s_i, increases logarithmically from $s_i = 0.1$ for nuclides with mass fraction $X_i \leqslant 10^{-5}$ to a possible maximum of $s_i = 30$ in arbitrary units.

The left column of Fig. 2 shows results for the pure deflagration setup, which used tracer particles of constant mass (see Section 3.1). The two cases containing the least number of tracer particles, 8^2 and 16^2, show globally poor agreement of the nuclide mass fractions with the reference values. The case containing 32^2 particles already shows good agreement of most Fe-peak nuclei, but many of the most abundant intermediate mass nuclei are under-produced on the 5%-level. Agreement with the reference values is only slightly improved by going to 64^2 tracer particles. Using 128^2 tracer particles finally reproduces the reference values of the most abundant nuclei globally on the 2%-level, with a few exceptions, most notably isotopes of Ne, Mg, and Al.

The right column of Fig. 2 shows results for the centrally ignited delayed detonation setup, which also used tracer particles of constant mass (see Section 3.2). Similar to the pure deflagration case, the two low resolution cases show globally poor agreement of the nuclide mass fractions with the reference values. Already the 32^2 tracer particle case shows rather good agreement with the high resolution reference run for the majority of the more abundant Fe-peak and intermediate mass nuclides. Compared to the pure deflagration, this delayed detonation agrees better with its references values for intermediate tracer particle numbers (i.e. 32^2 and 64^2). This can be traced back to the fact that the delayed detonation model synthesizes nuclides such as ^{28}Si, ^{32}S, ^{36}Ar or ^{40}Ca copiously during the detonation phase in a large volume where even the constant tracer particle mass implementation results in a tracer particle number density high enough to adequately sample the morphology. Notable exceptions to the better agreement are nuclides that are predominantly synthesized in the outer layers of the star during

---

[2] Small departures from exact powers of 2 were necessary to assure mass conservation and the constraint that tracer particles in the intermediate region all represent the same volume.
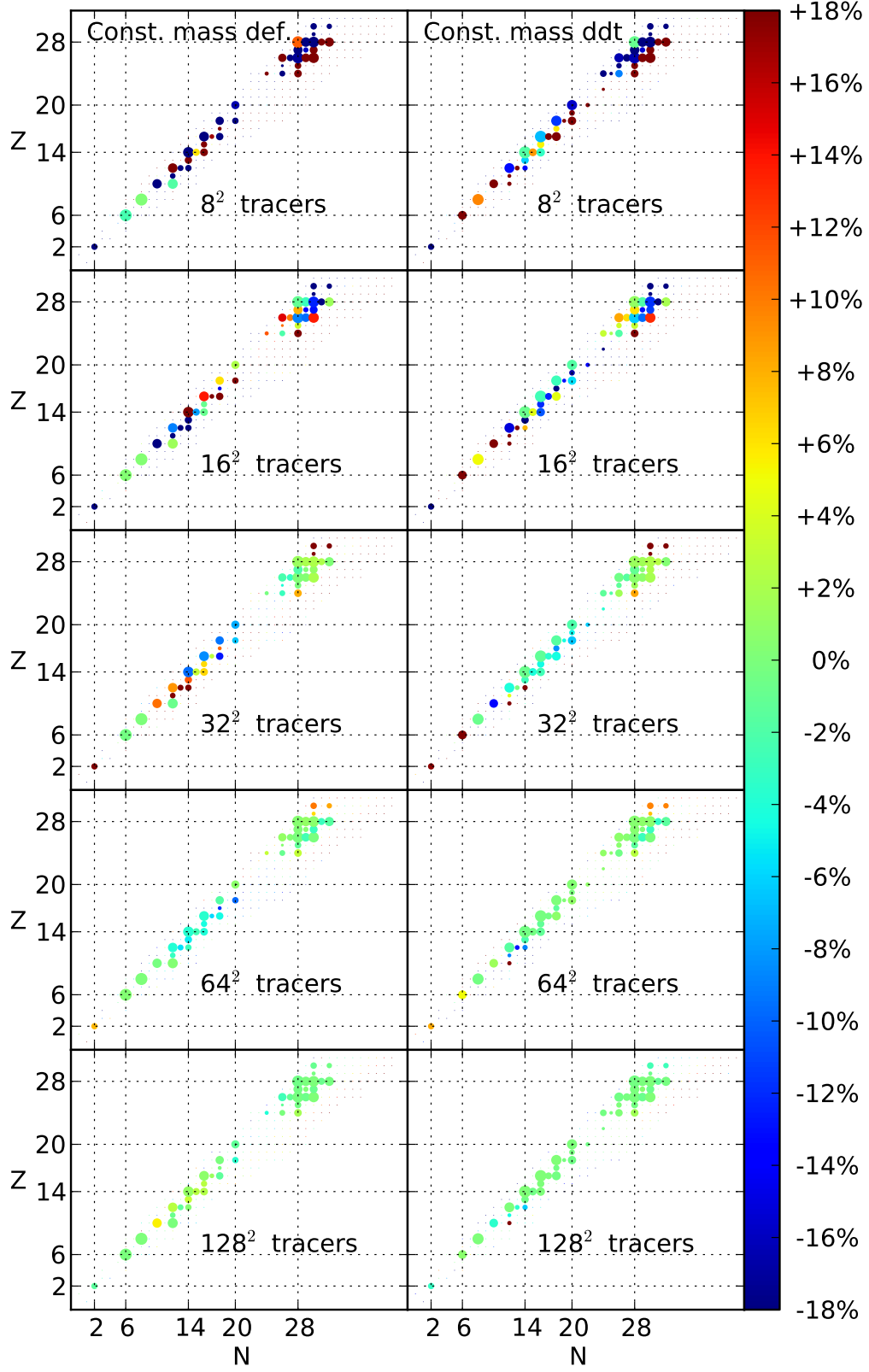
Figure 2. Final ($t = 10$ s) nuclide mass fraction differences $\left[\frac{X_i(N^2) - X_i(256^2)}{X_i(256^2)}\right]$ in percent for a sequence of increasing total tracer particle number compared with the highest resolved case containing 256^2 tracer particles. The underlying hydrodynamical simulation is the same central ignition pure deflagration for the left column (see Section 3.1) and the same centrally ignited delayed detonation model for the right column (see Section 3.2). In all cases the traditional constant tracer particle mass approach was used. The radius, s_i, of the markers increases with mass fraction X_i according to $s_i = \max\{0.1, 29.9[\log_{10}(X_i) + 5]/5 + 0.1\}$ in arbitrary units.
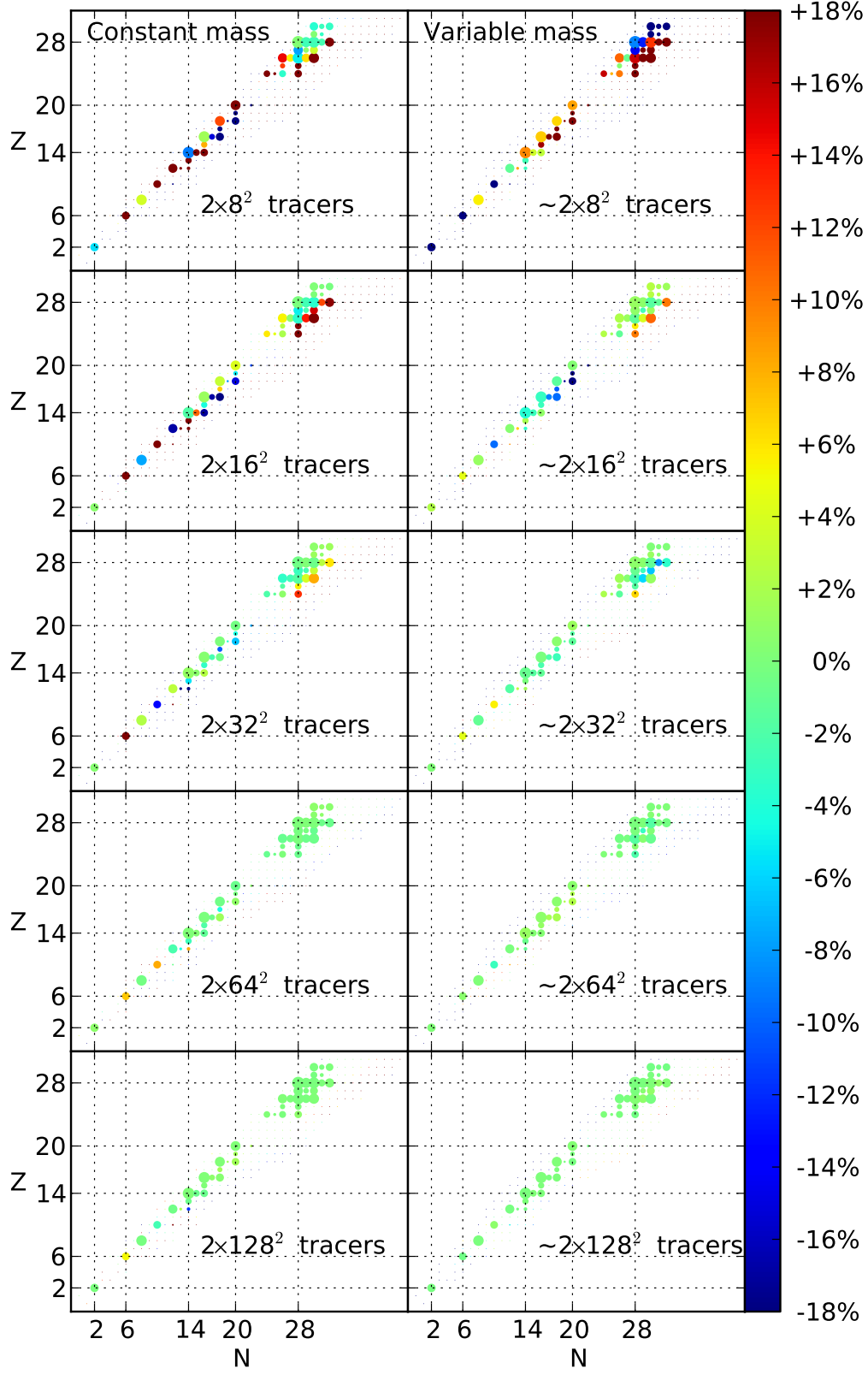
Figure 3. Final ($t = 10$ s) nuclide mass fraction differences $\left[\frac{X_i(2 \times N^2) - X_i(2 \times 256^2)}{X_i(2 \times 256^2)}\right]$ in percent for a sequence of increasing total tracer particle number compared with the highest resolved case containing 2×256^2 tracer particles. The underlying hydrodynamical simulation is the same multi-spot ignition delayed detonation model (see Section 3.3) for all cases. The left column is for tracer particles of constant mass, whereas for the right column the variable tracer mass approach was used (see Section 2.1 and Fig. 1). The radius, s_i, of the markers increases with mass fraction X_i according to $s_i = \max\{0.1, 29.9[\log_{10}(X_i) + 5]/5 + 0.1\}$ in arbitrary units.

the detonation phase, such as e.g. ^{20}Ne, ^{26}Mg or ^{27}Al (see the discussion of the multi-spot ignition delayed detonation model further below).

Fig. 3 shows results for the multi-spot ignition delayed detonation setup (see Section 3.1), with constant tracer particle mass runs in the left column, and variable tracer particle mass runs (see Section 2.1) in the right column. In spite of the differences in explosion model and nucleosynthetic yields, the sequence of the constant tracer mass case is qualitatively very similar to the centrally ignited delayed detonation (compare right column of Fig. 2 to the left column of Fig. 3). In all but the lowest resolution case, using a variable tracer mass approach results in a global improvement of the agreement with the reference values and improved convergence characteristics (compare right and left columns of Fig. 3). This improvement is due to the fact that the variable tracer mass approach alleviates the problem of low tracer particle density in the outer layers of the star inherent to the constant mass approach. Abundance gradients of problematic nuclides such as e.g. ^{20}Ne (see Fig. 4a), ^{26}Mg (see Fig. 4b) or ^{27}Al (see Fig. 5a), which are produced in an incomplete burn during the detonation phase at low density in the outer layers of the star, are much better resolved with the variable tracer mass implementation (compare right and left panels of Figs. 4a, 4b) and 5a. For nuclides which qualitatively agree equally well with their reference values for both constant and variable tracer mass cases, such as e.g. ^{28}Si, the variable tracer mass implementation results in a much improved spatial resolution of the abundance distribution morphology in the outer regions at the cost of a slightly worse resolution in the inner regions (see Fig. 5b).

5 SUMMARY AND CONCLUSIONS

We have performed a resolution study in the number of tracer particles required to converge on the integrated nucleosynthetic yield calculations for three different SN Ia explosion models. We find that for all explosion models, total nucleosynthetic yields appear to have converged (with few exceptions, see Section 4) for abundant nuclides with mass fractions $> 10^{-5}$ to better than 2% at 128 tracer particles per axis and direction. Agreement at better than the 5% level is already achieved for many of the most abundant nuclides at particle numbers as low as 32 per axis and direction.

Based on these results, we extrapolate that published yields from the literature (Travaglio et al. 2004, 2005; Brown et al. 2005; Röpke et al. 2006; Maeda et al. 2010) are based on sufficiently high numbers of tracer particles per axis that an adequate to good prediction of the most abundant nuclei is given. Furthermore, we have shown that for isotopes whose origin is near the surface of the WD, such as e.g. ^{20}Ne, ^{26}Mg or ^{27}Al, better convergence can be achieved if the constraint of constant tracer mass is relaxed and a choice for the tracer particle masses is made that better spatially resolves the outer layers.

The question of how many particles are required to get converged spectra and light curves from subsequent radiative transfer calculations is related. It seems plausible that a convergence of the total integrated yields is a necessary but not sufficient constraint. For the radiative transfer not only the total mass of a given isotope is important but also its lo-
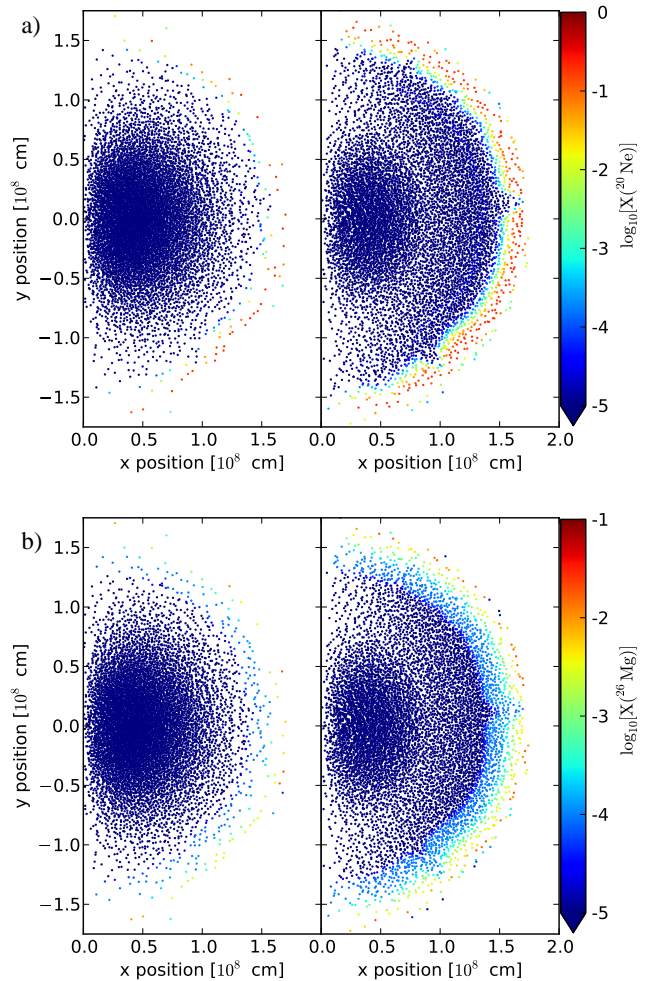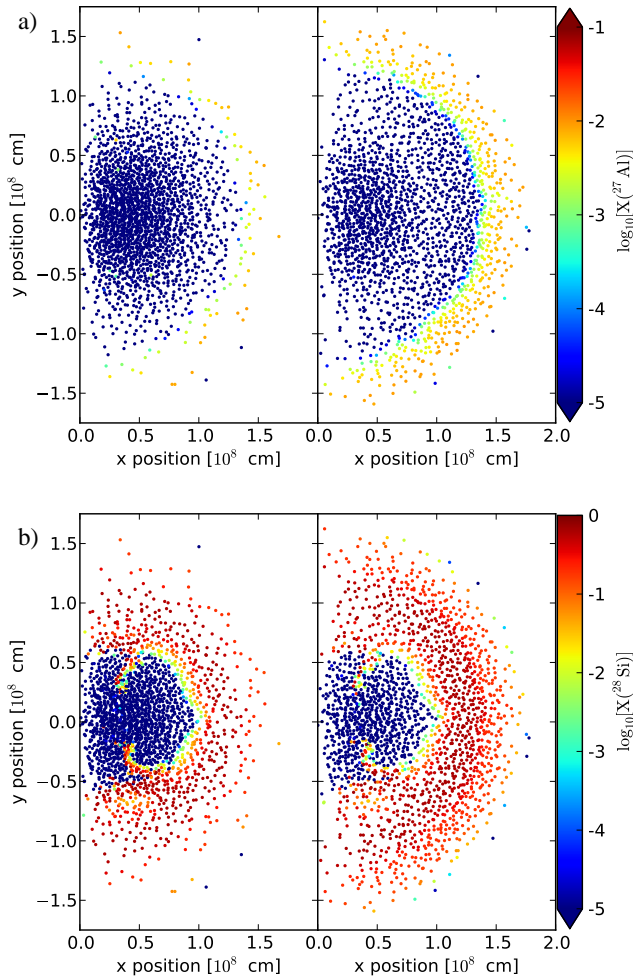

Figure 4. Initial spatial distribution of constant (left, $N = 8192$) and variable (right, $N = 8140$) mass tracer particles colored by the final mass fraction of ^{20}Ne (top panel) and ^{26}Mg (bottom panel) after freeze-out ($t = 10$ s).

cation in velocity space. It seems that the method of variable mass tracer particles is also promising in this context. Especially simulations where the nucleosynthesis is dominated by a detonation should greatly benefit from a variable tracer mass distribution, since the mass fractions in the inner regions vary smoothly radially and therefore a de-refinement in the inner part is not a high price to pay for increased resolution in the outer part. However, the reconstruction of an isotopic abundance for every computational cell of the radiative transfer calculation from the tracer particle distribution is not unique. The resultant spectra and light curves depend somewhat on particular choice of reconstruction algorithm used. These questions will likely be addressed in a future study.

Figure 5. Initial spatial distribution of constant (left, $N = 2048$) and variable (right, $N = 2024$) mass tracer particles colored by the final mass fraction of ^{27}Al (top panel) and ^{28}Si (bottom panel) after freeze-out ($t = 10$ s).

REFERENCES

Bravo E., García-Senz D., 2008, A&A, 478, 843
Brown E. F., Calder A. C., Plewa T., Ricker P. M., Robinson K., Gallagher J. B., 2005, Nuclear Physics A, 758, 451
Calder A. C., Townsley D. M., Seitenzahl I. R., Peng F., Messer O. E. B., Vladimirova N., Brown E. F., Truran J. W., Lamb D. Q., 2007, ApJ, 656, 313
Cappellaro E., Evans R., Turatto M., 1999, A&A, 351, 459
Colella P., Woodward P. R., 1984, Journal of Computational Physics, 54, 174
Colgate S. A., McKee C., 1969, ApJ, 157, 623
Fink M., Hillebrandt W., Röpke F. K., 2007, A&A, 476, 1133
Fink M., Röpke F. K., Hillebrandt W., Seitenzahl I. R., Sim S. A., Kromer M., 2010, ArXiv e-prints
Fryxell B. A., Müller E., Arnett W. D., 1989, MPA Green Report 449, Hydrodynamics and nuclear burning. Max-Planck-Institut für Astrophysik, Garching
Gamezo V. N., Khokhlov A. M., Oran E. S., 2005, ApJ, 623, 337
Gamezo V. N., Khokhlov A. M., Oran E. S., Chtchelkanova A. Y., Rosenberg R. O., 2003, Science, 299, 77
Gilfanov M., Bogdán Á., 2010, Nature, 463, 924
Hillebrandt W., Niemeyer J. C., 2000, ARA&A, 38, 191
Hoyle F., Fowler W. A., 1960, ApJ, 132, 565
Iwamoto K., Brachwitz F., Nomoto K., Kishimoto N., Umeda H., Hix W. R., Thielemann F.-K., 1999, ApJS, 125, 439
Jordan IV G. C., Fisher R. T., Townsley D. M., Calder A. C., Graziani C., Asida S., Lamb D. Q., Truran J. W., 2008, ApJ, 681, 1448
Kasen D., Röpke F. K., Woosley S. E., 2009, Nature, 460, 869
Khokhlov A. M., 1995, ApJ, 449, 695
Khokhlov A. M., Oran E. S., Wheeler J. C., 1997, ApJ, 478, 678
Kuchner M. J., Kirshner R. P., Pinto P. A., Leibundgut B., 1994, ApJ, 426, L89
Langanke K., Martinez-Pinedo G., 2000, Nuclear Physics A, 673, 481
Maeda K., Röpke F. K., Fink M., Hillebrandt W., Travaglio C., Thielemann F., 2010, ApJ, 712, 624
Meakin C. A., Seitenzahl I., Townsley D., Jordan G. C., Truran J., Lamb D., 2009, ApJ, 693, 1188
Mennekens N., Vanbeveren D., De Greve J. P., De Donder E., 2010, ArXiv e-prints
Nagataki S., Hashimoto M., Sato K., Yamada S., 1997, ApJ, 486, 1026
Niemeyer J. C., 1999, ApJ, 523, L57
Nomoto K., Thielemann F.-K., Yokoi K., 1984, ApJ, 286, 644
Pakmor R., Kromer M., Röpke F. K., Sim S. A., Ruiter A. J., Hillebrandt W., 2010, Nature, 463, 61
Pankey T. J., 1962, PhD thesis, Howard University.
Plewa T., 2007, ApJ, 657, 942
Plewa T., Calder A. C., Lamb D. Q., 2004, ApJ, 612, L37
Rauscher T., Thielemann F.-K., 2000, Atomic Data and Nuclear Data Tables, 75, 1
Reinecke M., Hillebrandt W., Niemeyer J. C., 1999, A&A, 347, 739
Reinecke M., Hillebrandt W., Niemeyer J. C., 2002a, A&A, 386, 936
Reinecke M., Hillebrandt W., Niemeyer J. C., 2002b, A&A, 391, 1167
Röpke F. K., 2005, A&A, 432, 969
Röpke F. K., 2007, ApJ, 668, 1103
Röpke F. K., Gieseler M., Reinecke M., Travaglio C., Hillebrandt W., 2006, A&A, 453, 203
Röpke F. K., Hillebrandt W., 2005, A&A, 431, 635
Röpke F. K., Hillebrandt W., Schmidt W., Niemeyer J. C., Blinnikov S. I., Mazzali P. A., 2007, ApJ, 668, 1132
Röpke F. K., Niemeyer J. C., 2007, A&A, 464, 683
Röpke F. K., Woosley S. E., Hillebrandt W., 2007, ApJ, 660, 1344
Ruiter A. J., Belczynski K., Fryer C., 2009, ApJ, 699, 2026

Seitenzahl I. R., Meakin C. A., Lamb D. Q., Truran J. W., 2009a, ApJ, 700, 642

Seitenzahl I. R., Meakin C. A., Townsley D. M., Lamb D. Q., Truran J. W., 2009b, ApJ, 696, 515

Seitenzahl I. R., Meakin C. A., Townsley D. M., Truran J. W., Lamb D. Q., 2008, in T. Suda, T. Nozawa, A. Ohnishi, K. Kato, M. Y. Fujimoto, T. Kajino, & S. Kubono ed., Origin of Matter and Evolution of Galaxies Vol. 1016 of American Institute of Physics Conference Series, Nucleosynthesis in surface detonation Type Ia supernovae. pp 472–474

Seitenzahl I. R., Townsley D. M., Peng F., Truran J. W., 2009c, Atomic Data and Nuclear Data Tables, 95, 96

Sim S. A., Röpke F. K., Hillebrandt W., Kromer M., Pakmor R., Fink M., Ruiter A. J., Seitenzahl I. R., 2010, ApJ, 714, L52

Thielemann F.-K., Hashimoto M.-A., Nomoto K., 1990, ApJ, 349, 222

Thielemann F.-K., Nomoto K., Hashimoto M.-A., 1996, ApJ, 460, 408

Thielemann F.-K., Nomoto K., Yokoi K., 1986, A&A, 158, 17

Townsley D. M., Calder A. C., Asida S. M., Seitenzahl I. R., Peng F., Vladimirova N., Lamb D. Q., Truran J. W., 2007, ApJ, 668, 1118

Travaglio C., Hillebrandt W., Reinecke M., 2005, A&A, 443, 1007

Travaglio C., Hillebrandt W., Reinecke M., Thielemann F.-K., 2004, A&A, 425, 1029

Travaglio C., Kifonidis K., Müller E., 2004, New Astronomy Review, 48, 25

Truran J. W., Arnett W. D., Cameron A. G. W., 1967, Canadian Journal of Physics, 45, 2315

Vladimirova N., Weirs G. V., Ryzhik L., 2006, Combustion Theory Modelling, 10, 727

Woosley S. E., 2007, ApJ, 668, 1109

Woosley S. E., Kerstein A. R., Sankaran V., Aspden A. J., Röpke F. K., 2009, ApJ, 704, 255